Influence of transition elements (Zr, V and Mo) on microstructure and tensile properties of AlSi8Mg casting alloys

Zhan Zhang[1*], Anil Arici[1], Francis Breton[2], X.-Gant Chen[1]

[1] Department of Applied Science, University of Quebec at Chicoutimi,
Saguenay (QC), Canada, G7H 2B1
[2] Arvida Research and Development Centre, Rio Tinto,
Saguenay (QC), Canada, G7S 4K8
*Corresponding author: zhan_zhang@uqac.ca

Abstract

The influence of the additions of transition elements (Zr, V and Mo) on microstructure, precipitation behavior and tensile properties of Al-8%Si-0.3%Mg permanent mould castings were investigated. It reveals that the presence of the transition elements increased the solute concentration in aluminum matrix, refined eutectic Si particles, and reduced the length and aspect ratio of intermetallic phases in as-cast microstructure. Moreover, the transition element addition promoted the formation of solute cluster and increased the number density of β" precipitates and dispersoids during T6 heat treatment. The additions of Zr, V and Mo considerably improved the tensile strengths and elongation in both as-cast and T6 conditions. The effects of the combined addition of Zr, V and Mo on the microstructure, precipitation behavior and tensile properties were stronger than that of the addition of Zr and V.

Keywords: Al-Si-Mg casting alloy, precipitates, dispersoids, transition elements, microstructure, mechanical properties.

1. Introduction

Al-Si-Mg casting alloys are widely used in the transport industries due to their many outstanding attributes including excellent castability and good mechanical properties [1,2]. The presence of magnesium in the hypoeutectic Al-Si alloys provides high strengths mainly by precipitation strengthening and solute solution strengthening [1,2]. Many researches have been performed to improve both strength and ductility of the alloys to meet the increasing demand of mechanical performance from industries by increasing precipitates and dispersoids, as well as modifying eutectic silicon and intermetallic compounds [3-11]. To promote the precipitation strengthening, Al-Si-Mg alloys are

usually solution-treated and artificially aged to form nanosized precipitates by the decomposition of supersaturated solid solution [2]. The precipitation sequence in Al-Si-Mg alloys during aging treatment is known as follows: supersaturated solute solution → Mg and Si clusters → GP zones → β" → β' → β-Mg_2Si [12-14]. The formation of the main strengthening phases, β" and β' precipitates, depends on the solute diffusion of Mg and Si in the aluminum matrix [15,16]. However, the alloying elements, particularly transition elements such as Zr and V, may influence solute diffusion because they interact with vacancies in aluminum during heat treatment [15,16]. Voncina et al. [17] reported that Zr addition accelerated precipitation of Q-$Al_5Cu_2Mg_8Si_6$ and β"-MgSi in AlSi10Mg alloy during aging treatment. Yuan et al. [18] found that Zn addition increased the number density of β"-MgSi precipitates in Al-Mg-Si-Cu-Mn alloys.

Transition elements such as Mn, Zr, V, and Mo, generally have low solid solubility and low diffusivity in aluminum, leading to the precipitation of stable phases in aluminum alloys during heat treatment [2-4]. Kasprzak et al. [3] found that the additions of Ti, Zr and V in Al–7%Si–1%Cu–0.5%Mg alloy generated rod-shaped Al_3(Zr,V,Ti) dispersoids in grain interiors during heat treatment. Farkoosh et al. [6] reported that a number of α-Al(Fe,Mo)Si dispersoids were generated in the grain interiors during solution treatment with a minor addition of Mo (0.3 wt.%) in Al–7Si–0.5Cu–0.3Mg alloy. Those dispersoids enhanced the mechanical properties by hindering the dislocation movement during loading [3-6]. Zaman et al. [4] reported that the additions of Zr, Ni, V and Cr, promoted the formation of intermetallic compounds, such as $(AlSi)_3$(CrVTi), AlSiV, $(AlSi)_3$(ZrTi), $(AlSi)_3$(CrV), Al_9FeNi, etc. in Al-10%Si alloys during solidification. The micron-size intermetallic particles distributed in intergranular regions, resulting in the increase of

tensile strengths but at the cost of ductility at ambient and elevated temperatures. In addition, some transition elements are able to modify eutectic Si [4,7,11]. The combined addition of Zr and Gd, for example, could significantly refine eutectic silicon and change its morphology from plate-like to fibrous, attributed to the increase of constitutional undercooling and the inhibition of the growth of eutectic Si during solidification [7].

Despite numerous previous investigations, the roles of the transition elements such as Zr and V and Mo on precipitation behavior of strengthening phases and mechanical properties in Al-Si-Mg casting alloys have not be fully understood. Since the solid solubility of Zr, V, and Mo in aluminum is quite low, the combined addition of these transition elements is more effective than the individual addition for the improvement of the mechanical properties of the alloys [4,8,9]. The present study aimed to investigate the influence of combined addition of Zr and V, as well as Zr, V and Mo on the microstructure evolution and mechanical properties of an Al-8%Si-Mg alloy under as-cast and heat-treated conditions. Several characterization techniques, such as optical microscopy, scanning and transmission electron microscopies, differential scanning calorimetry and electrical conductivity measurement, were used to characterize and quantify the as-cast and heat-treated microstructures.

2. Experimental Methods

Three Al-8%Si-0.3%Mg experimental alloys were prepared, including the base alloy and two modified alloys. The base alloy was one variant of Aural^{TM} casting alloy series (7-10%Si, 0.2-0.5%Mg, 0.5%Mn), which are widely used in automotive industry. One modified alloy contained both Zr and V, and the other had the combined addition of Zr, V and Mo. Commercially pure Al (99.7%), pure Mg (99.9%), Al-50%Si, Al-25%Mn, Al-

25%Fe, Al-5%V, Al-15%Zr and Al-10%Mo master alloys were used in the alloy preparation. For each batch, approximately 3 kg of materials were melted in an electrical resistance furnace. The melt was kept at 750 ºC for 30 min and degassed for 15 min.

Figure 1. the copper permanent mold used in the experiments.

The melt was then poured into a copper permanent mold (Figure 1) preheated at 250 ºC. The dimension of the cast plates is 100 mm x 80 mm with a thickness of 4 mm. The cast plate has an average cooling rate of approximately 18 ºC/s. Some of the cast plates were heat-treated in T6 temper, which consists of the solution treatment at 540 °C for 2 h followed by water quench, and then artificial aging at 170 °C for 4 h. The chemical compositions of the experimental alloys analyzed by an optical emission spectrometer are listed in Table 1.

Table 1. Chemical composition of the experimental alloys (wt.%).

Alloy	Si	Mn	Mg	Fe	Ti	Sr	Zr	V	Mo	Al
base	8.15	0.52	0.39	0.13	0.09	0.011	0.00	0.00	0.00	bal.
B	8.19	0.52	0.30	0.14	0.09	0.013	**0.17**	**0.33**	0.00	bal.
C	7.68	0.51	0.30	0.14	0.05	0.012	**0.19**	**0.25**	**0.15**	bal.

Conventional metallographic polishing method was used to prepare the samples for microstructure observation. The polished samples were etched by 0.5% HF in deionized water for 35 seconds to reveal the distribution of dispersoids. A scanning electron

microscope (SEM, JSM-6480LV) equipped with an energy dispersive X-ray spectrometer (EDS) was used to analyze the microstructure of these experimental alloys. A transmission electron microscope (TEM, JEM-2100) equipped with an energy dispersive X-ray spectroscopy (EDS) was applied to examine precipitates and dispersoids in detail. TEM foils were prepared in a twin-jet electropolisher using a solution of 30% nitric acid in methanol at -20 ºC. Convergent-beam electron diffraction (CBED) patterns were used to measure the thicknesses of TEM foils for the calculation of number density of dispersoids and precipitates. An optical image analyzer with CLEMEX JS-2000, PE4.0 software was employed to quantitatively characterize the phase features on optical, SEM and TEM images. For Si particles, 25 optical images with 500x magnifications for each sample were taken, and then the characteristics of the silicon particles in those optical images were statistically analyzed using the image analyzer. For intermetallic particles, 25 backscattered SEM images with 500x magnification for each sample were statistically analyzed with the image analyzer. The characteristics of needle-like β”-MgSi precipitates, such as the number density and size, were analyzed with the methods developed in Ref. [19], and 6-8 TEM bright-field images with 50,000x magnification for each T6 sample were quantitatively analyzed.

The tensile tests were carried out at room temperature using an Instron universal testing machine according to the ASTM B557. Sub-size tensile test samples with a gage length of 25 mm and an overlength of 100mm based on ASTM B557, were machined from the cast plates. The tensile properties, namely the ultimate tensile strength (UTS), yield strength (YS) at a 0.2% offset strain and fracture elongation (El), were reported as the average values of six test plates. The electrical conductivity of the alloys was measured by

Sigmascope SMP10 unit to assess the solute level in aluminum matrix. The average value was calculated from minimum ten measurements for each sample. A differential scanning calorimetry (DSC, Mettler Teledo Model III) was use to analyze precipitation kinetics at a heating rate of 10°C/min under argon protective atmosphere on the solution-treated samples of approximate 15 milligrams and 4 mm in diameter, which were stored at -6°C before DSC tests to avoid natural aging. A high purity aluminum reference sample was used in the DSC test.

3. Results and Discussion

3.1 Effect of Zr, V and Mo on microstructure in as-cast and T6 conditions

The as-cast microstructures of the experimental alloys are shown in Figure 2, which generally consisted of α-Al dendrite cells/grains, eutectic silicon, primary Mg_2Si and various intermetallic phases distribute in the interdendritic regions. The identification of intermetallic phases was based on the results of SEM-EDS, phase morphologies and the information of our previous work and published literature [6, 9, 20-23]. Typical SEM-EDS spectra of intermetallic phases are shown in Figure 3. In the base alloy (Figure 2a and b), in addition to primary Mg_2Si, needle-like Fe/Mn-bearing $Al_{15}(FeMn)_3Si_2$ intermetallic compound distributed in the interdendritic regions (Figure 3a). In the B alloy (Figure 2c), a similar $Al_{15}(FeMnV)_3Si_2$ intermetallic was observed (Figure 3b), in which some V substituted Fe and Mn in $Al_{15}(FeMn,)_3Si_2$. In addition, a small amount of short plate-like $(AlSi)_3(ZrTi)$ intermetallic appeared (Figure 3c). In the C alloy (Figure 2d), two similar intermetallic phases $(AlSi)_3(ZrTi)$ and $Al_{15}(FeMnVMo)_3Si_2$ were observed. $Al_{15}(FeMnVMo)_3Si_2$ is a variant of Fe/Mn-bearing $Al_{15}(FeMn)_3Si_2$ (Figure 3d), in which

some V and Mo substitute Fe and Mn. Table 2 lists the phase characteristics of eutectic Si and intermetallic phases based on the image analysis results. It reveals that the sizes of the eutectic silicon particles in the B and C alloys are slightly finer than that in the base alloy, while the length and aspect ratio of the intermetallic phases in the B and C alloys are shorter and smaller than that in the base alloy. In addition, the transition element additions increase the volume fraction of intermetallics in the B and C alloys by ~ 10 vol.% compared to the base alloy.

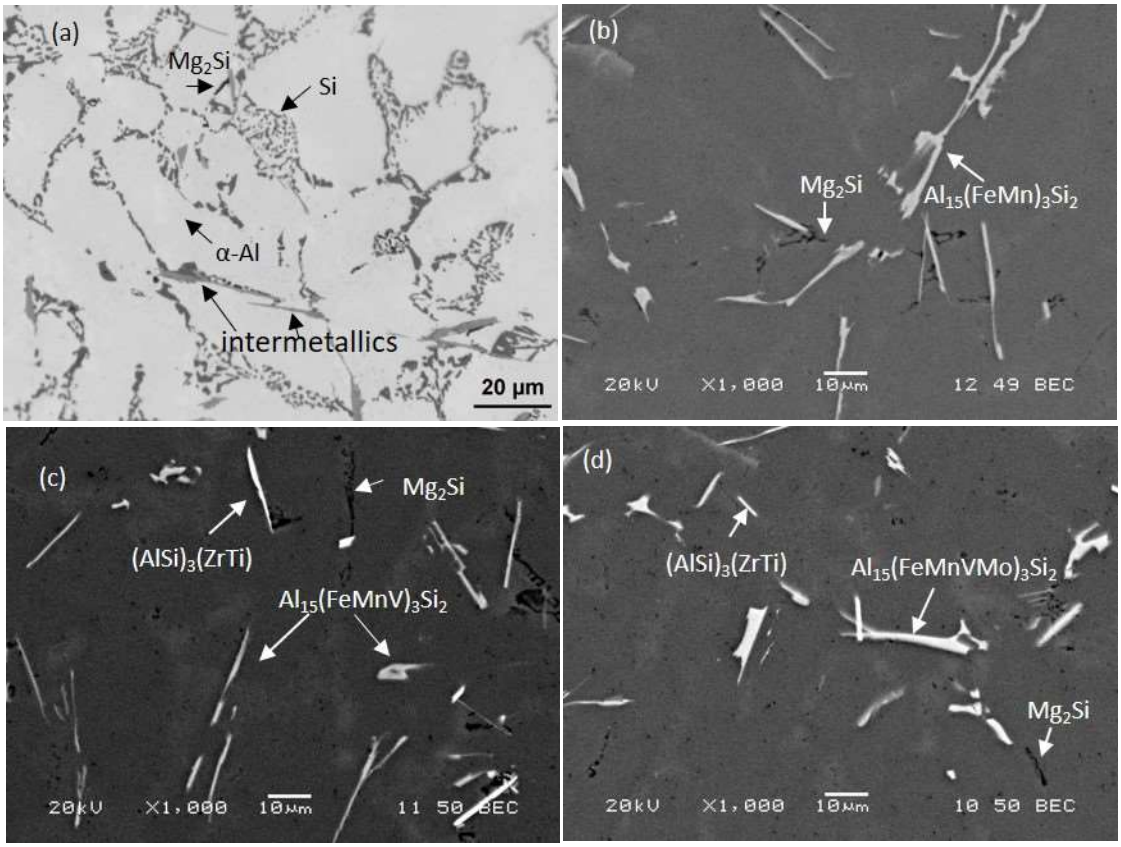

Figure 2. Optical as-cast microstructure of the base alloy (a), SEM backscattered image of the base alloy (b), the B alloy (c) and the C alloy (d).

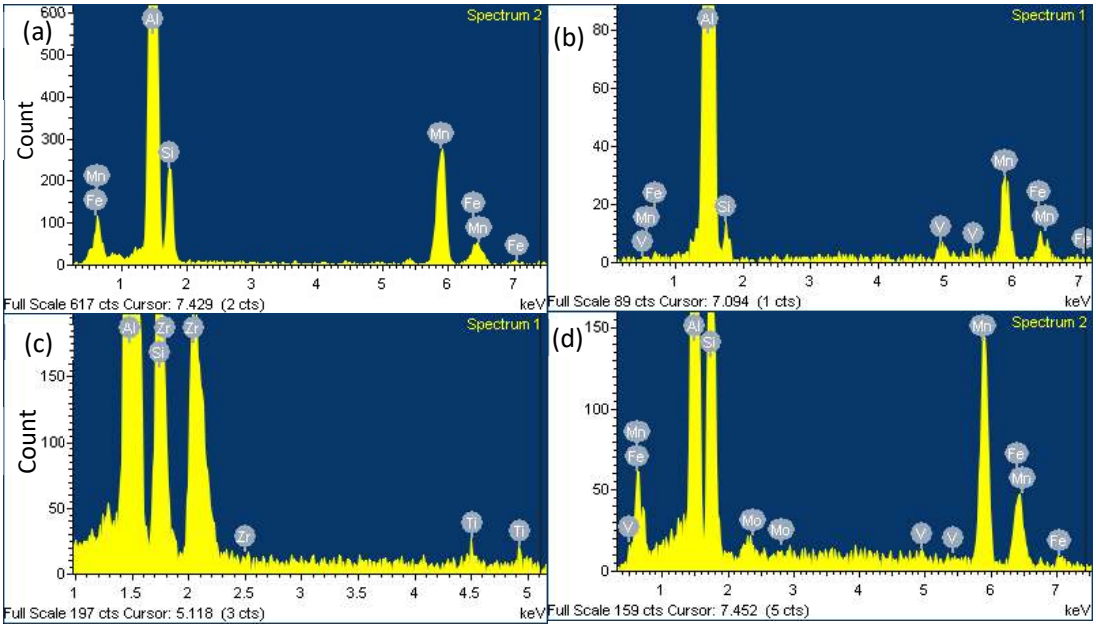

Figure 3. Typical EDS spectra of intermetallic phases, (a) $Al_{15}(FeMn)_3Si_2$ intermetallic in the base alloy (Figure 2b), (b) $Al_{15}(FeMnV)_3Si_2$ and (c) $(AlSi)_3(ZrTi)$ intermetallics in the B alloy (Figure 2c), (d) $Al_{15}(FeMnVMo)_3Si_2$ intermetallic in the C alloy (Figure 2d).

Table 2. Measured characteristics of eutectic Si and intermetallic phases in as cast condition with standard division

Alloy	Equivalent diameter of eutectic Si (μm)	Average length of intermetallic phases (μm)	Average aspect ratio of intermetallic phases
base	1.7 ± 0.6	25.4 ± 4.1	3.6 ± 0.7
B	1.4 ± 0.5	18.8 ± 5.2	2.9 ± 0.4
C	1.4 ± 0.5	15.3 ± 4.8	3.1 ± 0.4

Figure 4a shows a typical solution-treated microstructure in the example of the C alloy. During the solution treatment, the eutectic Si particles became spheroidized, whereas the Fe/Mn-bearing intermetallic phases of all three alloys were partially dissolved and fragmented (see the inset in Figure 4a). However, the length and aspect ratio of the intermetallic particles in the B and C alloys were shorter and smaller than that in the base alloy. For example, the length of the intermetallic particles in the base alloy is 20.1 ± 3.3 μm, 14.2 ± 5.2 μm in the B alloy and 11.7 ± 4.6 μm in the C alloy, respectively, while the

aspect ratio of the fragments/particles is 3.1 ± 0.5 in base ally, 2.5 ± 0.4 in the B alloy, and 2.4 ± 0.5 in C ally. It is also interesting to find that the size of spheroidized Si particles in the B and C alloys was smaller than that of the base alloy. For example, the Si equivalent diameter is 2.0 ± 0.6 μm in the base alloy, 1.7 ± 0.4 μm in B ally, and 1.5 ± 0.5 μm in the C alloy. It indicates that the addition of the transition elements refined the silicon particles and reduced the length and aspect ratio of the intermetallic particles in T6 samples, which results in the decrease of local stress concentration on these particles, consequently the improvement of strength and ductility. In addition, a number of dark dots distributed in the grain interiors, which were the thermally stable dispersoids generated during solution treatment due to the presence of relatively high Mn content (0.5%) in the experimental alloys, for example, the type of α-Al(FeMn)Si dispersoids , which are thermally stable at room and elevated temperature. TEM was used to examine the dispersoids in detail. In the base alloy, rod-like dispersoids were observed (Figure 4b). Based on the TEM-EDS result (Fig. 5a), the phase morphologies, and the information from the literature [9, 23-27], the dispersoids were identified to be α-Al(FeMn)Si. In the B alloy, two types of submicron-sized dispersoids were found (Figure 4c). The former was $(AlSi)_3(ZrTi)$ dispersoids (Figure 5b) [9, 23] and the latter was α-Al(FeMnV)Si dispersoids (Figure 5c), which was a variant of α-Al(FeMn)Si where some V substituted Fe and Mn [9]. In the C alloy (Figure 4d), two types of submicron-sized dispersoids similar to the B alloy were observed. They were $(AlSi)_3(ZrTi)$ and α-Al(FeMnVMo)Si. The latter was a variant of α-Al(FeMn)Si, in which some V and Mo replaced Fe and Mn (Figure 5d) [6, 23, 24].

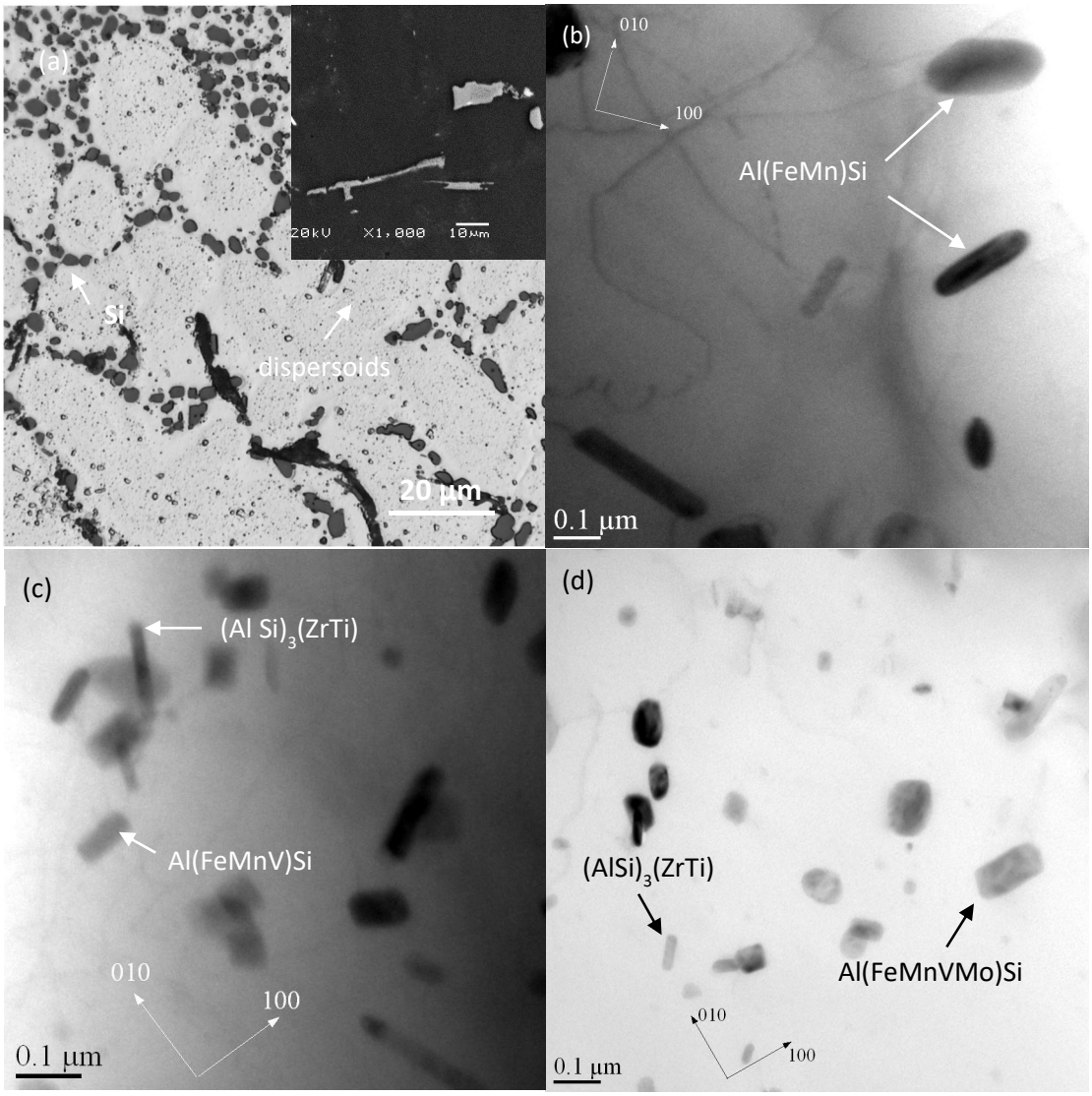

Figure 4. Optical image of the solution-treated microstructure in the C alloy and the inset showing the intermetallic particles (a), bright-field TEM images showing dispersoids in base (b), B (c) and C (d) alloys after the solution treatment.

The characteristics of dispersoids in the three alloys in term of the size (equivalent radius r_d), number density (N_d) and volume fraction (f_d) are listed in Table 3. The size of dispersoids in the B and C alloys was smaller than that in the base alloy, while the number density and volume fraction of the B and C alloys were higher than that of the base alloy.

For example, the number density of dispersoids was ~4 times higher in the B alloy and ~8 times higher in the C alloy compared with the base alloy, respectively. Because of the similarity in the size range, two types of dispersoids were treated as the same strengthening phase in the present work.

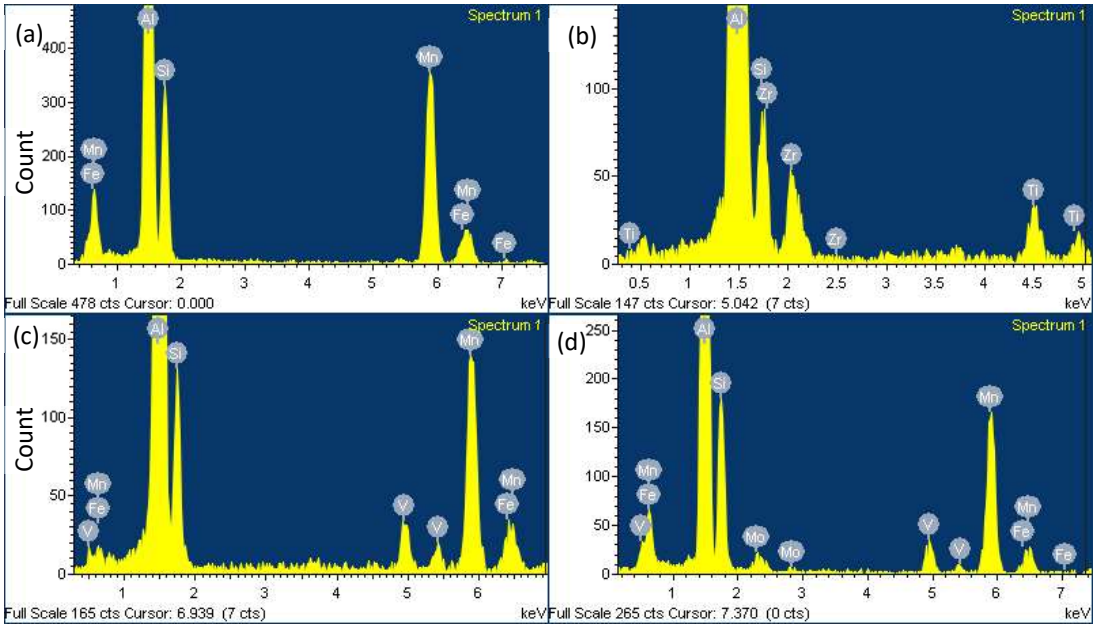

Figure 5. Typical TEM-EDS spectra of dispersoids, (a) α-Al(FeMn)Si in the base alloy (Figure 4b), (b) $(AlSi)_3(ZrTi)$ and (c) α-Al(FeMnV)Si in the B alloy (Figure 4c), (d) α-Al(FeMnVMo)Si in the C alloy (Figure 4d).

Figure 6 shows the typical needle-like precipitates distributed on $\{100\}_\alpha$ plans of aluminum in the base and C alloys after aging treatment. The dark dots were the cross sections of the needle-like precipitates. It is known that the precipitates formed during aging treatment are the metastable phases of Mg_2Si in Al-Si-Mg alloys [19,28]. The nanosized precipitates in the three experimental alloys belong to the type of β"-MgSi based on their dimension and morphology [28]. The β"-MgSi precipitates were quantitatively characterized, and the results are presented in Table 3. Apparently, the size (cross section

and length) of β" precipitates in the base alloy was slightly larger than that in transition-element-containing alloys, while the number density of β" precipitates in the transition-element-containing alloys was significantly higher. For example, the number density of precipitates was ~12% higher in the B alloy and ~24% higher in the C alloy than that in the base alloy, respectively.

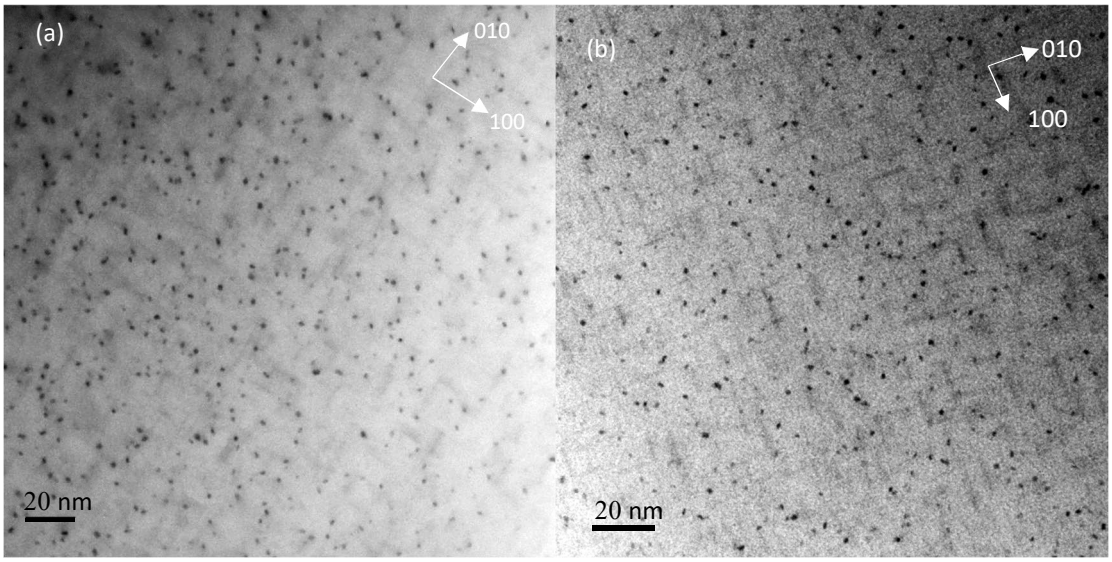

Figure 6. Bright-field TEM images of β" precipitates (a) in the base, (b) in the C alloy after aging treatment.

Table 3. Quantitative results of dispersoids and precipitates in the experimental alloys with standard deviation.

Alloy	Dispersoids			β" precipitates		
	Number density, N_d, (μm^{-3})	Equivalent radius, r_d, (nm)	Volume fraction, f_d, (%)	Number density, N_v, (μm^{-3})	Average area of cross section, A_{pr}, (nm^2)	Average length, l_{pr}, (nm)
Base	17.1 ± 6.8	54.2 ±12.1	0.81%	8.9 x 10^4	4.8 ± 0.2	21.3 ±2.6
B	72.6 ± 3.4	33.4 ±3.6	0.87%,	1.0 x 10^5	4.7 ± 0.1	20.8 ±1.7
C	144.3 ± 4.3	29.6 ±4.2	0.95%,	1.1 x 10^5	4.6 ± 0.1	20.4 ±1.5

3.2 DSC results

The precipitation behaviors of the experimental alloys were investigated using differential scanning calorimetry (DSC) on the solution-treated samples. Figure 7 shows the typical DSC curves of the base and C alloys. The DSC curve of the B alloy is not shown here because it was similar to that of the C alloy. There were several exothermic peaks, H, A, B, and C, in the base alloy. In the C alloy, in addition to those peaks, an exothermic peak G appeared at the temperature lower than H peak. The peak characteristics in term of the peak onset temperature (O_p), peak temperature (P_p) and integrated area of peak (A_p), are listed in Table 4. Based on the literature [12-14], the peaks H, A, B, and C in the DSC curves of the experimental alloys corresponded to the formation of GP zone, β", β', and β, respectively, while the peak G represented the formation of the solute clusters of Mg and Si. The peak G appeared at 89 °C in the B alloy and at 92 °C in the C alloy, but no peak G was observed in the base alloy. The integrated peak areas of the GP zones and β" in the B and C alloys were larger than that of the base alloy, while their onset temperatures were lower. It indicates that the addition of transition elements affected the thermal dynamic process of the precipitation, and promoted the formation of the solute clusters, GP-zone and β" precipitates in Al-Si-Mg alloys.

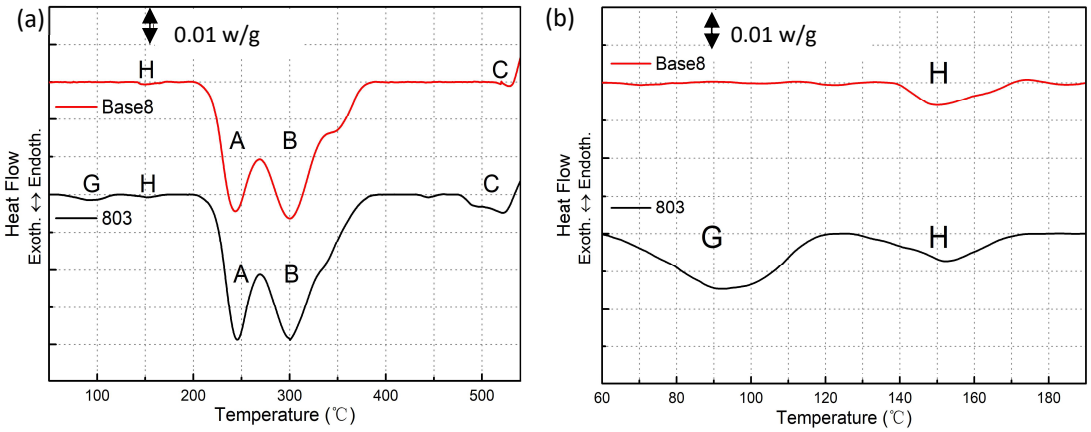

Figure 7. Differential scanning calorimetry (DSC) curves of the base and the C alloys (a), and their enlarged view from 60 °C to 110 °C (b).

Table 4. Characteristics of exothermic peaks in the experimental alloys.

Alloy	G (cluster)	H (GP)	A (β")
	P_p°C	O_p°C /P_p°C/A_p J/g	O_p°C /P_p°C/A_p J/g
base	-	140/150/1.4	202/240/59.5
B	89	129/152/2.2	201/248/63.6
C	92	128/152/2.7	202/244/65.8

3.3 Effect of Zr, V and Mo on tensile properties

Figure 8 shows the tensile properties of the experiment alloys in as-cast condition. The results revealed that the YS, UTS and El of the transition-element-containing alloys (B and C) were significantly higher than that of the base alloy. Compared to the base alloy, the increases were by 24% in YS, 27% in UTS, and 33% in El in the B alloy, and 27% in YS, 32% in UTS and 61% in El in the C alloy, respectively. It is evident that the addition of the transition elements significantly improved both strengths and elongation in as-cast condition.

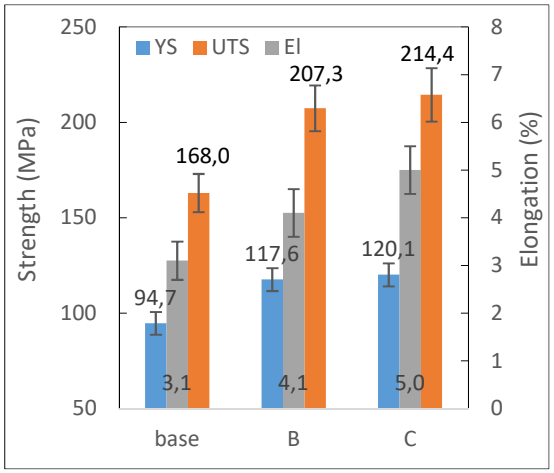

Figure 8. Tensile properties of the experimental alloys in as-cast condition.

The tensile properties of the experimental alloys in T6 condition are shown in Figure 9. The strengths and elongation of the transition-element-containing alloys were higher than that of the base alloy, especially for the C alloy. For example, the YS, UTS and

El of the C alloy were approximately 20%, 23% and 115% higher than that of the base alloy, while they are 13.2%, 6% and 38.5% higher for the B alloy, respectively. This indicates that strengthening effect of the combined addition of Zr, V and Mo is higher than that of Zr and V. In addition, comparing the tensile properties in as-cast and T6 conditions, it is apparent that T6 strongly improved the strengths of the alloys owing to the precipitation of nanosized β", but decreased the ductility in some extent.

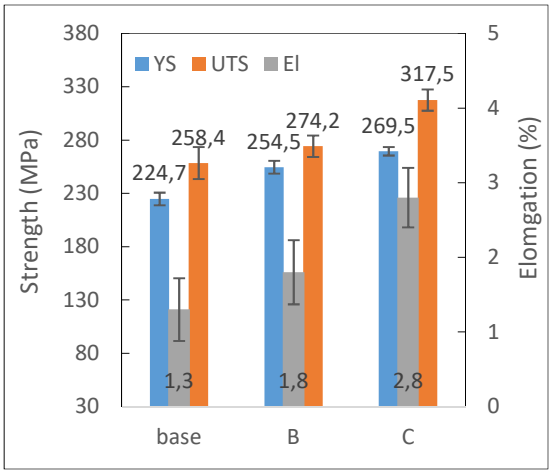

Figure 9. Tensile properties of the experimental alloys in T6 condition.

3.4 Discussion

The addition of transition elements, Zr, V and Mo, in AlSi8Mg alloy considerably improve the tensile properties in both as-cast and T6 conditions (Figures 8 and 9). During solidification, the presence of a small amount of transition elements could increase the constitutional undercooling and the inhibition of the growth of eutectic Si during solidification [7]. A part of transition elements was also involved in the formation of intermetallic phases $(AlSi)_3(ZrTi)$, $Al_{15}(FeMnV)_3Si_2$ and $Al_{15}(FeMnVMo)_3Si_2$), resulting in the refining of eutectic silicon particles and intermetallic compounds in the as-cast microstructure (Table 2). This refining is beneficial to reduce the local stress concentration

during loading, consequently resulting in the improvement of the mechanical properties, especially for ductility [1,2,29]. In fact, the elongation was increased by 33% in the B alloy (Zr and V addition) and 61% in the C alloy (Zr, V and Mo addition) (Figure 7). The rest transition elements were dissolved in the aluminum to form the supersaturated solid solution. The electrical conductivity is often used to indicate the concentration level of solutes in aluminum alloys. The lower electrical conductivity is, the higher level of solute concentration in the materials. The electrical conductivities measured in as-cast and T6 conditions are listed in Table 5. In the as-cast condition, the electrical conductivities of the transition-element-containing alloys (B and C) were obviously lower than that in the base alloy, and the electrical conductivity of the C alloy was the lowest among three experiment alloys. This indicates that the solute levels of the transition-element-containing alloys were remarkably higher than that of the base alloy, providing a higher solid solution strengthening. In T6 condition, the difference of electrical conductivities in three alloys were very small. It can be concluded that the improvement of as-cast tensile properties due to the transition element addition is attributed to the combined contribution of solid solution strengthening, the formation of intermetallic compounds, and refined eutectic-Si and intermetallic compounds. The solid solution strengthening and the formation of intermetallic compounds make predominate contribution to the strength, while the refinements of Si and intermetallic particles are especially beneficial to the improvement of the ductility.

Table 5. Electrical conductivity in as-cast and T6.

Alloy	Electrical Conductivity (MS/m)	
	As-cast	T6
base	20.13	20.66
B	17.50	19.13
C	16.50	19.03

During aging treatment in T6 temper, nanosized β"-MgSi were precipitated out in the aluminum matrix as the main strengthening phase (Figure 6). In the precipitation process, the Mg and Si solutes segregate and first form cluster through solid diffusion, and these clusters further grow and gradually construct their crystal structures to form of metastable phases (β" and β') [12,13,15]. The formation of clusters is mainly controlled by solute-vacancy diffusion mechanism [15,16]. The solute-vacancy bindings of V, Zr in aluminum are -0.33 eV and -0.28 eV, and for Mo it is between -0.28 eV (Zr) and 0.07 eV (Ag), respectively, while the values of Si and Mg are 0.08 eV and ~0 eV, respectively [16]. Negative solute-vacancy binding indicates that solutes repel vacancies, while positive solute-vacancy bindings show an energetically favorable binding [16,30]. During aging, the solutes of the transition elements repel their neighbor vacancies, which could increase the likelihood of the formation of clusters and precipitates through diffusion kinetics process [31]. In fact, the DSC curves showed an obvious peak G for the cluster formation in the transition-element-containing alloys (Figure 7), indicating that more clusters were formed in these alloys (B and C). Moreover, the integrated areas of peak A (β" precipitation) of the transition-element-containing alloys were larger than that of the base alloy (Figure

7a and Table 5), showing that more β" precipitates were formed due to the transition element addition, which is consistent with the TEM observation (Figure 6 and Table 3). It was also reported that the cluster formed at 70°C in pre-precipitation process can increase the number density of β" precipitates because the formed Mg and Si clusters have the potential to become the nucleus of β" precipitates in Al-Mg-Si alloys [13]. In addition, during solution treatment, the solid solution supersaturated by the transition elements (Mn, Zr, V and Mo) was decomposed, and the thermally stable dispersoids were precipitated in the aluminum matrix of the experimental alloys (Figure 4). The addition of transition elements (Zr, V and Mo) promoted the formation of dispersoids and increased the number density and volume fraction of dispersoids (Table 3), providing a complementary strengthening to the aluminum matrix. It can be concluded that the enhanced precipitation strengthening of β" and complementary strengthening of dispersoids induced by the transition elements are the main factors to improve the mechanical properties of the experimental alloys in T6 condition. In addition, the refined Si and intermetallic particles are also contributed to the improvement of the strength and ductility of the alloys containing transition elements. Apparently, the combined addition of Zr, V and Mo exhibited the stronger effect on the microstructure and mechanical properties than that of the addition of Zr and V.

4. Conclusions

In this study, the effects of the additions of transition elements (Zr, V and Mo) on microstructure and mechanical properties of Al-8%Si-0.3%Mg permanent mould castings were investigated in as-cast and T6 conditions. The following conclusions can be drawn:

1. In as-cast condition, the additions of Zr, V and Mo increased both tensile strength and ductility of the Al-8%Si-0.3%Mg alloys, namely 24-27% in YS and 27-32% in UTS, and elongation, 33-61%, which were mainly attributed to the enhanced solid solution strengthening and the refining of eutectic Si particles and intermetallic compounds.
2. In T6 condition, the additions of transition elements promoted the formation of Mg and Si solute clusters and increased the number density of β" precipitates and dispersoids in the experimental alloys. The enhanced precipitation strengthening of β" and complementary strengthening of dispersoids were the main factors to improve the tensile properties of the Al-8%Si-0.3%Mg alloys. In addition, the refined Si and intermetallic particles due to the addition of the transition elements were also contributed to the improvement of the tensile properties of the alloys, especially for the ductility.
3. The effects of the combined addition of Zr, V and Mo on the eutectic Si, intermetallic phases, precipitation behavior and tensile strength and ductility were stronger than that of the additions of Zr and V.

Disclosure statement

No potential conflict of interest was reported by the author(s).

Acknowledgments

The authors would like to acknowledge the financial support of the Natural Sciences and Engineering Research Council of Canada (NSERC) under the Grant No. CRDPJ 514651-

17 and Rio Tinto Aluminum through the NSERC Industry Research Chair in the Metallurgy of Aluminum Transformation at University of Quebec at Chicoutimi.

Reference

[1] Zolotorevsky VS, Belov NA, Glazoff MV. Casting Aluminum Alloys, Elsevier, Oxford, 2007; 247-262

[2] Totten GE, Mackenzie DC. Handbook of Aluminum, Vol. 1, Marcel Dekker Inc. New York, 2003; 591-611

[3] Kasprzak W, Amirkhiz BS, Niewczas M, Structure and properties of cast Al-Si based alloy with Zr-V-Ti additions and its evaluation of high temperature performance. Journal of alloys and compounds. 2014; 595: 67-79

[4] Zamania M, Morinib L, Ceschinib L, Seifeddinea S. The role of transition metal additions on the ambient and elevated temperature properties of Al-Si alloys. Materials Science & Engineering A, 2017; 693: 42-50.

[5] Shaha SK, Czerwinski F, Kasprzak W, Friedman J, and Chen DL. Effect of Cr, Ti, V, and Zr Micro-additions on Microstructure and Mechanical Properties of the Al-Si-Cu-Mg Cast Alloy, Metallurgical and Materials Transactions A, 2016; 47A: 2396-2409.

[6] Farkoosh AR, Chen XG, Pekguleryuz M, Dispersoid strengthening of a high temperature Al–Si–Cu–Mg alloy via Mo addition, Materials Science & Engineering A, 2014; 620: 181-189

[7] Liu W, Xiao W, Xu C, Liu M, Ma C. Synergistic effects of Gd and Zr on grain refinement and eutectic Si modification of Al-Si cast alloy, Materials Science & Engineering A, 2017; 693: 93-100.

[8] Rakhmonov J, Timelli G, Bonollo F. The effect of transition elements on high-temperature mechanical properties of Al-Si foundry alloys - a Review, Advanced Engineering materials, 2016; 18: 1096-1105.

[9] Rakhmonov J, Timelli G, Fabrizi A, F. Bonollo, Effect of V and Zr microalloying, and heat treatment on microstructure and mechanical properties of secondary Al-7Si-3Cu-0.3Mg alloy, International Journal of Materials Research, 2018; 109: 1099-1112.

[10] Asghar Z, Requena G, Boller E. Three-dimensional rigid multiphase networks providing high temperature strength to cast AlSi10Cu5Ni1-2 piston alloys, Acta Materialia, 2011; 59: 6420-6432.

[11] Pourbahari B, Emamy M, Effect of La intermetallics on the structure and tensile properties of thin section gravity die-cast A357 Al alloy, Materials and design, 2016; 94: 111-120.

[12] Edwards GA, Stiller K, Dunlop GL, Couper MJ. The precipitation sequence in Al-Mg-Si alloys, Acta Materialia, 1998; 46: 3893-3902.

[13] Murayma M, Hpno K, Pre-precipitate cluster and precipitation process in Al-Mg-Si alloys, Acta Materialia, 1999; 47: 1537-1548.

[14] Dutta I, Allen SM. A calorimetric study of precipitation in commercial aluminum alloy 6061, Journal of materials science letters, 1991;10:323-326.

[15] Porter DA, Easterling KE. M.Y. Sherif, Phase transformations in metals and alloys, CRC Press, Taylor & Francis Group, 2011, 251-289

[16] Wolverton C, Solute–vacancy binding in aluminum, Acta Materialia, 2007;55:5867-5872

[17] Vončina M, Medved J, Kores S, Xiec P, Schumacher P, Li J. Precipitation microstructure in Al-Si-Mg-Mn alloy with Zr additions, Materials Characterization, 2019; 155:1-8.

[18] Yuan B, Guo M, Wu Y, Zhang J, Zhuang, L. Lavernia EJ. Influence of treatment pathways on the precipitation behaviors of Al-Mg-Si-Cu-(Zn)-Mn alloys, Journal of Alloys and Compounds, 2019;797:26-38.

[19] Andersen SJ. Quantification of the Mg_2Si β″ and β′ phases in AlMgSi alloys by transmission electron microscopy, Metallurgical and Materials Transactions A, 1995;26(8):1931-1937.

[20] Rakhmonov J, Timelli G, Bonollo F. Characterization of the solidification path and microstructure of secondary Al-7Si-3Cu-0.3Mg alloy with Zr, V and Ni additions", Materials Characterization, 2017;128:100-108.

[21] Qian H, Zhu D, Hu CF, Jiang XS. Effects of Zr additive on microstructure, mechanical properties, and fractography of Al-Si Alloy, Materials, 2018;8:1-10.

[22] Biswas P, Patra S, Mondal MK. Structure-property correlation of eutectic Al-12.4Si alloys with and without zirconium (Zr) addition, International Journal of Cast metals Research, 2020;33:134-145

[23] Elgallad EM, Liu K, Zhang Z, Chen XG. Effect of transition elements on dispersoid formation and elevated-temperature mechanical properties in 6082 aluminum alloy, Philosophical Magazine, Part A: Materials Science, 2021;101:96-116.

[24] Farkoosh AR, Chen XG, Pekguleryuza M. Interaction between molybdenum and manganese to form effective dispersoids in an Al–Si–Cu–Mg alloy and their influence on creep resistance, Materials Science & Engineering A, 2015;627:127-138.

[25] Liu K, Chen XG. Development of Al-Mn-Mg 3004 alloy for applications at elevated temperature via dispersoid strengthening, Materials and Design, 2015;84:340-350.

[26] Li YJ, Arnberg L. Quantitative study on the precipitation behavior of dispersoids in DC-cast AA3003 alloy during heating and homogenization, Acta Materialia, 2003;51: 3415-3428.

[27] Li Z, Zhang Z, Chen XG. Improvement in the mechanical properties and creep resistance of Al-Mn-Mg 3004 alloy with Sc and Zr addition, Materials Science & Engineering A, 2018;729:196–207

[28] Andersen SJ, Zandbergen HW, Jansen J, Traeholt C, Tundal U, Reiso O. The crystal structure of the β" phase in Al-Mg-Si alloys", Acta Materialia, 1998;46(9):3283-3298.

[29] Dieter GE, Mechanical Metallurgy, McGraw-Hill Book Company, New York, 1988. 362-368

[30] Hoshino T, Zeller R, Dederichs PH, Local-density-functional calculation for defect interactions in Al, Physical Review B. 1996;53:8971-8974.

[31] Peng J, Bahl S, Shyam A, Haynes JA, Shin D. Solute-vacancy clustering in aluminum Acta Mater. 196 (2020) 747-758.

Tables with captions

Table 1. Chemical composition of the experimental alloys (wt.%).

Alloy	Si	Mn	Mg	Fe	Ti	Sr	Zr	V	Mo	Al
base	8.15	0.52	0.39	0.13	0.09	0.011	0.00	0.00	0.00	bal.
B	8.19	0.52	0.30	0.14	0.09	0.013	**0.17**	**0.33**	0.00	bal.
C	7.68	0.51	0.30	0.14	0.05	0.012	**0.19**	**0.25**	**0.15**	bal.

Table 2. Measured characteristics of eutectic Si and intermetallic phases in as cast condition with standard division

Alloy	Equivalent diameter of eutectic Si (μm)	Average length of intermetallic phases (μm)	Average aspect ratio of intermetallic phases
base	1.7 ± 0.6	25.4 ± 4.1	3.6 ± 0.7
B	1.4 ± 0.5	18.8 ± 5.2	2.9 ± 0.4
C	1.4 ± 0.5	15.3 ± 4.8	3.1 ± 0.4

Table 3. Quantitative results of dispersoids and precipitates in the experimental alloys with standard deviation.

Alloy	Dispersoids			β" precipitates		
	Number density, N_d, (μm^{-3})	Equivalent radius, r_d, (nm)	Volume fraction, f_d, (%)	Number density, N_v, (μm^{-3})	Average area of cross section, A_{pr}, (nm^2)	Average length, l_{pr}, (nm)
Base	17.1 ± 6.8	54.2 ±12.1	0.81%	8.9 x 10^4	4.8 ± 0.2	21.3 ±2.6
B	72.6 ± 3.4	33.4 ±3.6	0.87%,	1.0 x 10^5	4.7 ± 0.1	20.8 ±1.7
C	144.3 ± 4.3	29.6 ±4.2	0.95%,	1.1 x 10^5	4.6 ± 0.1	20.4 ±1.5

Table 4. Characteristics of exothermic peaks in the experimental alloys.

Alloy	G (cluster)	H (GP)	A (β")
	P_p°C	O_p°C /P_p°C/A_p J/g	O_p°C /P_p°C/A_p J/g
base	-	140/150/1.4	202/240/59.5
B	89	129/152/2.2	201/248/63.6
C	92	128/152/2.7	202/244/65.8

Table 5. Electrical conductivity in as-cast and T6.

Alloy	Electrical Conductivity (MS/m)	
	As-cast	T6
base	20.13	20.66
B	17.50	19.13
C	16.50	19.03

Figures

Figure 1. the copper permanent mold used in the experiments.

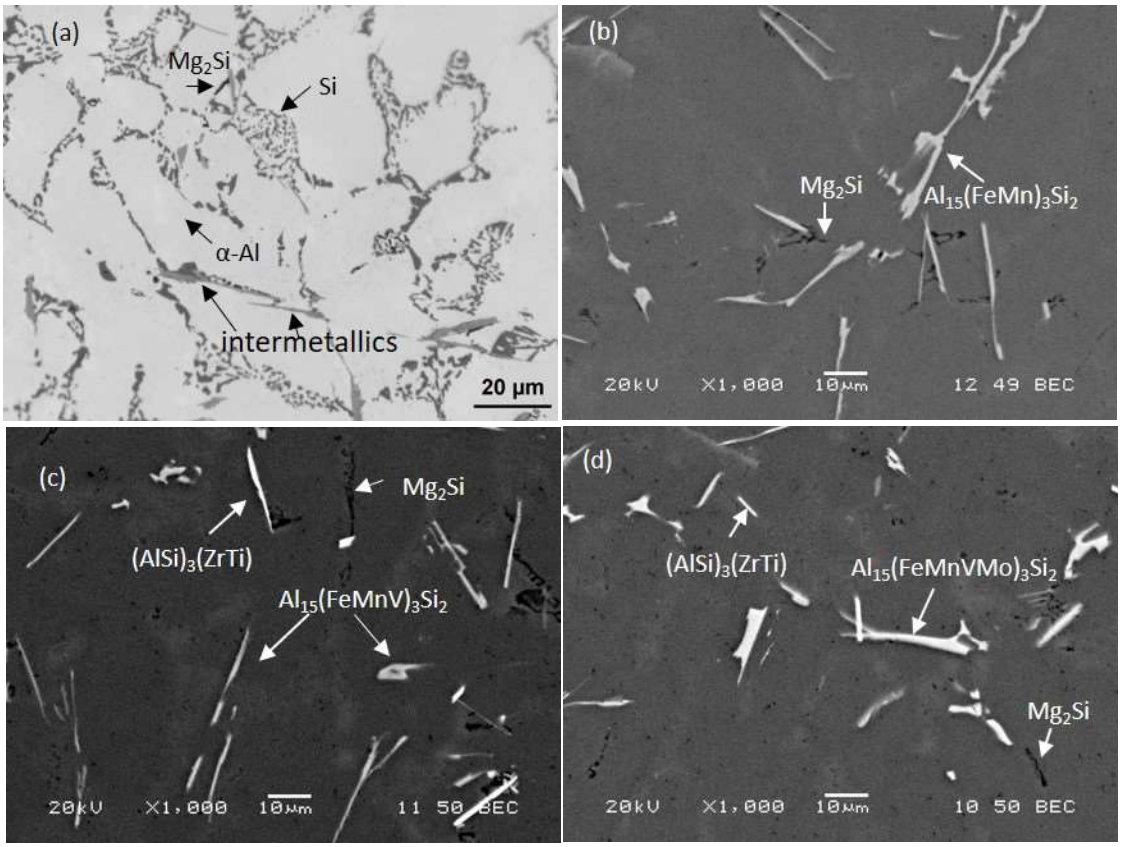

Figure 2. Optical as-cast microstructure of the base alloy (a), SEM backscattered images of the base alloy (b), the B alloy (c) and the C alloy (d).

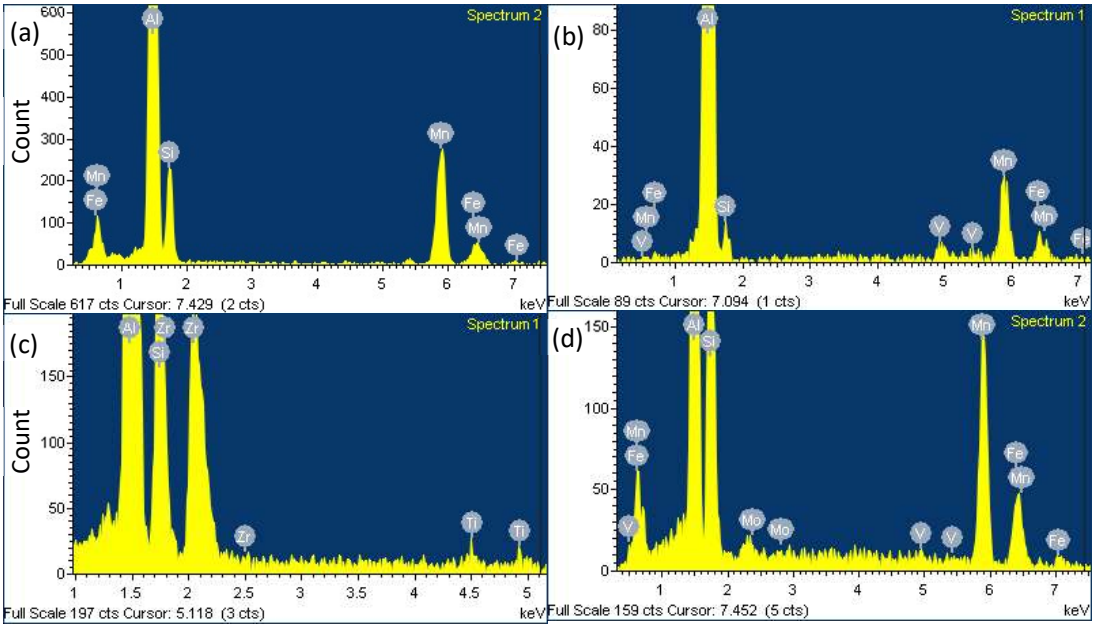

Figure 3. Typical EDS spectra of intermetallic phases, (a) $Al_{15}(FeMn)_3Si_2$ intermetallic in the base alloy (Figure 2b), (b) $Al_{15}(FeMnV)_3Si_2$ and (c) $(AlSi)_3(ZrTi)$ intermetallics in the B alloy (Figure 2c), (d) $Al_{15}(FeMnVMo)_3Si_2$ intermetallic in the C alloy (Figure 2d).

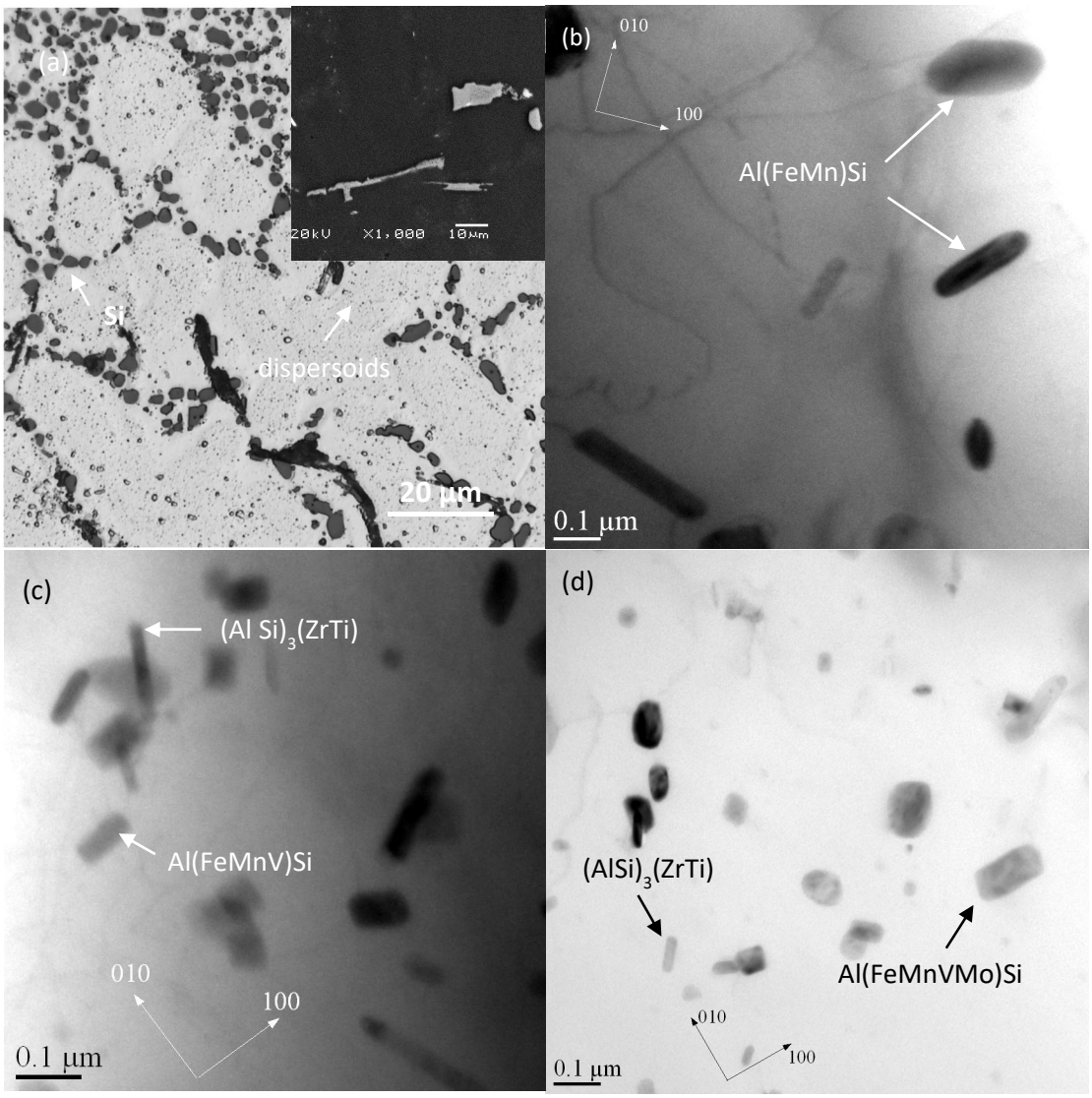

Figure 4. Optical image of the solution-treated microstructure in the C alloy and the inset showing the intermetallic particles (a), bright-field TEM images showing dispersoids in base (b), B (c) and C (d) alloys after the solution treatment.

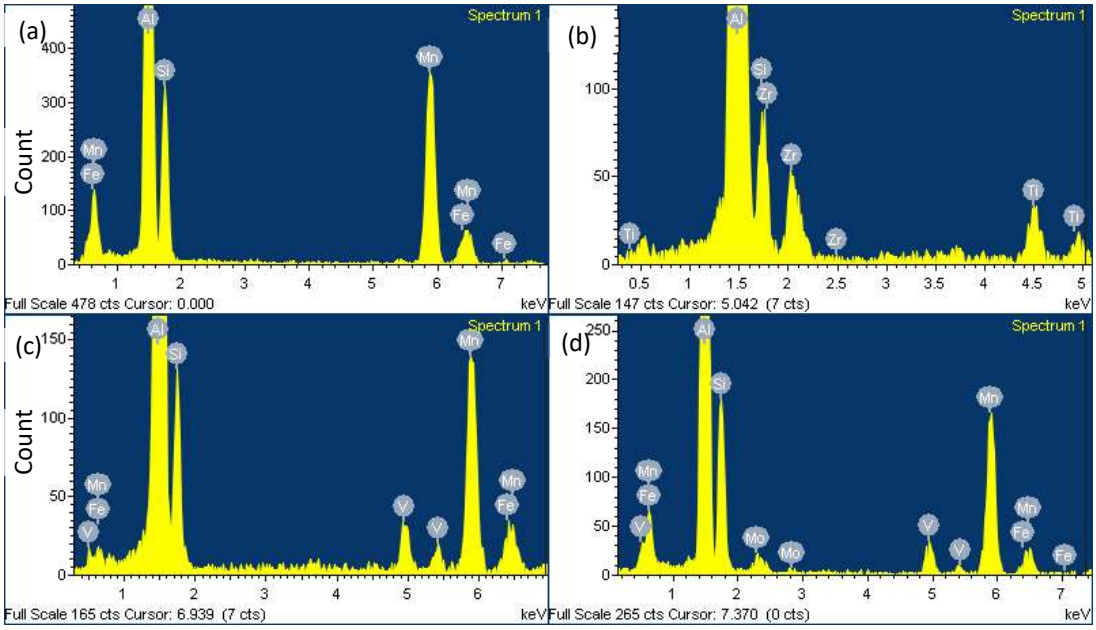

Figure 5. Typical TEM-EDS spectra of dispersoids, (a) α-Al(FeMn)Si in the base alloy (Figure 4b), (b) $(AlSi)_3(ZrTi)$ and (c) α-Al(FeMnV)Si in the B alloy (Figure 4c), (d) α-Al(FeMnVMo)Si in the C alloy (Figure 4d).

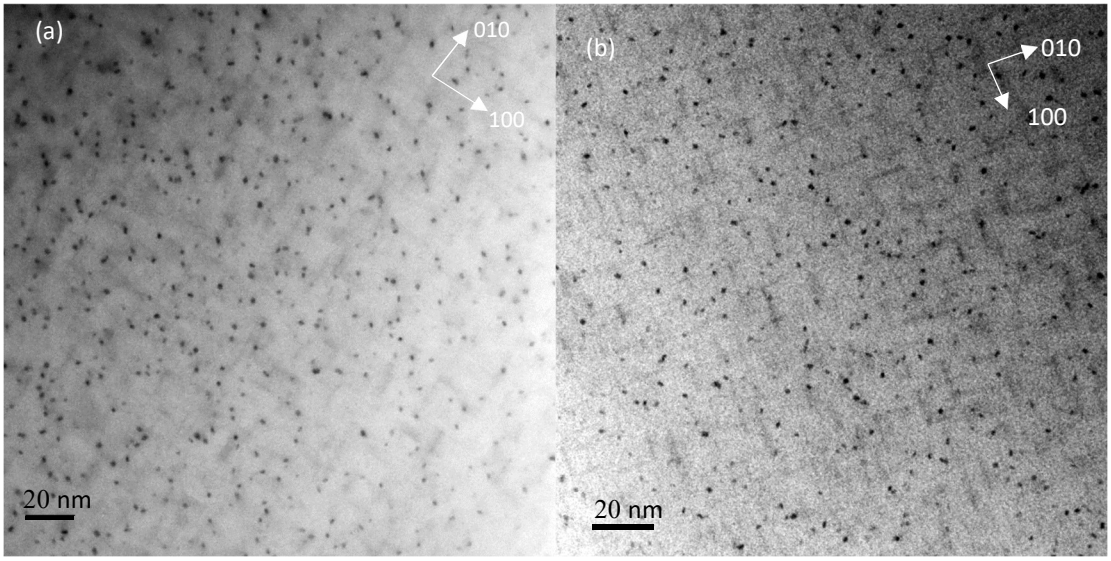

Figure 6. Bright-field TEM images of β" precipitates (a) in the base, (b) in the C alloy after aging treatment.

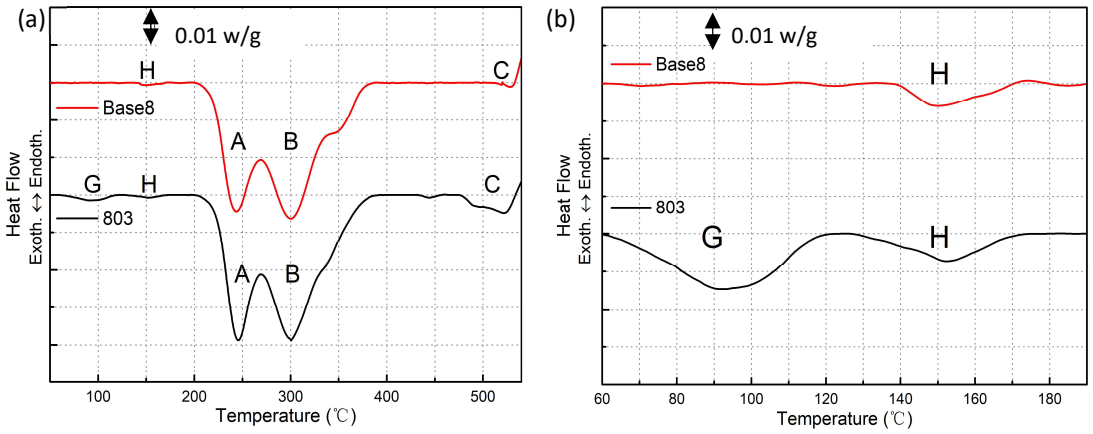

Figure 7. Differential scanning calorimetry (DSC) curves of the base and C alloys (a), and their enlarged view from 60 °C to 110 °C (b).

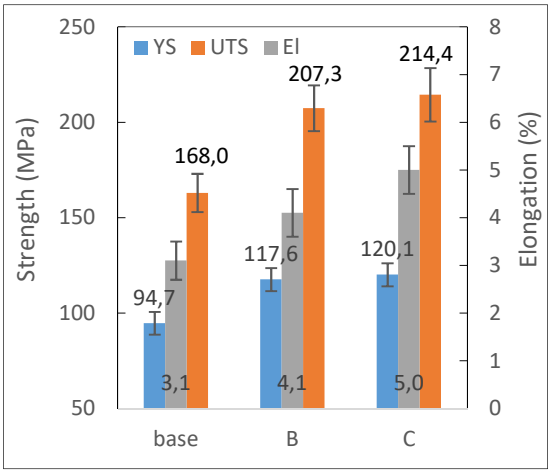

Figure 8. Tensile properties of the experimental alloys in as-cast condition.

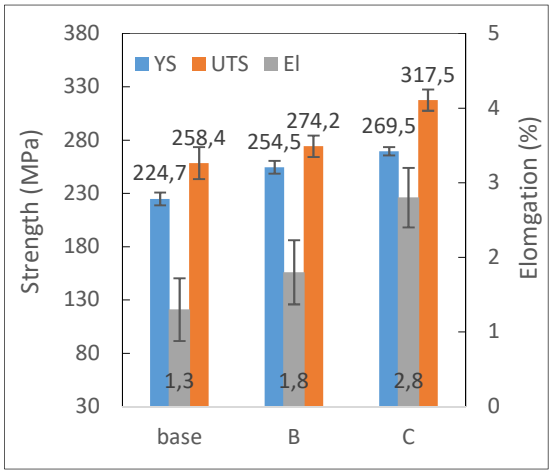

Figure 9. Tensile properties of the experimental alloys in T6 condition.

Figure Captions

Figure 1. the copper permanent mold used in the experiments.

Figure 2. Optical as-cast microstructure of the base alloy (a), SEM backscattered images of the base alloy (b), the B alloy (c) and C alloy (d).

Figure 3. Typical EDS spectra of intermetallic phases, (a) $Al_{15}(FeMn)_3Si_2$ intermetallic in the base alloy (Figure 2b), (b) $Al_{15}(FeMnV)_3Si_2$ and (c) $(AlSi)_3(ZrTi)$ intermetallics in the B alloy (Figure 2c), (d) $Al_{15}(FeMnVMo)_3Si_2$ intermetallic in the C alloy (Figure 2d).

Figure 4. Optical image of the solution-treated microstructure in the C alloy and the inset showing the intermetallic particles (a), bright-field TEM images showing dispersoids in base (b), B (c) and C (d) alloys after the solution treatment.

Figure 5. Typical TEM-EDS spectra of dispersoids, (a) α-Al(FeMn)Si in the base alloy (Figure 4b), (b) $(AlSi)_3(ZrTi)$ and (c) α-Al(FeMnV)Si in the B alloy (Figure 4c), (d) α-Al(FeMnVMo)Si in the C alloy (Figure 4d).

Figure 6. Bright-field TEM images of β" precipitates (a) in the base, (b) in the C alloy after aging treatment.

Figure 7. Differential scanning calorimetry (DSC) curves of the base and C alloys (a), and their enlarged view from 60 °C to 110 °C (b).

Figure 8. Tensile properties of the experimental alloys in as-cast condition.

Figure 9. Tensile properties of the experimental alloys in T6 condition.